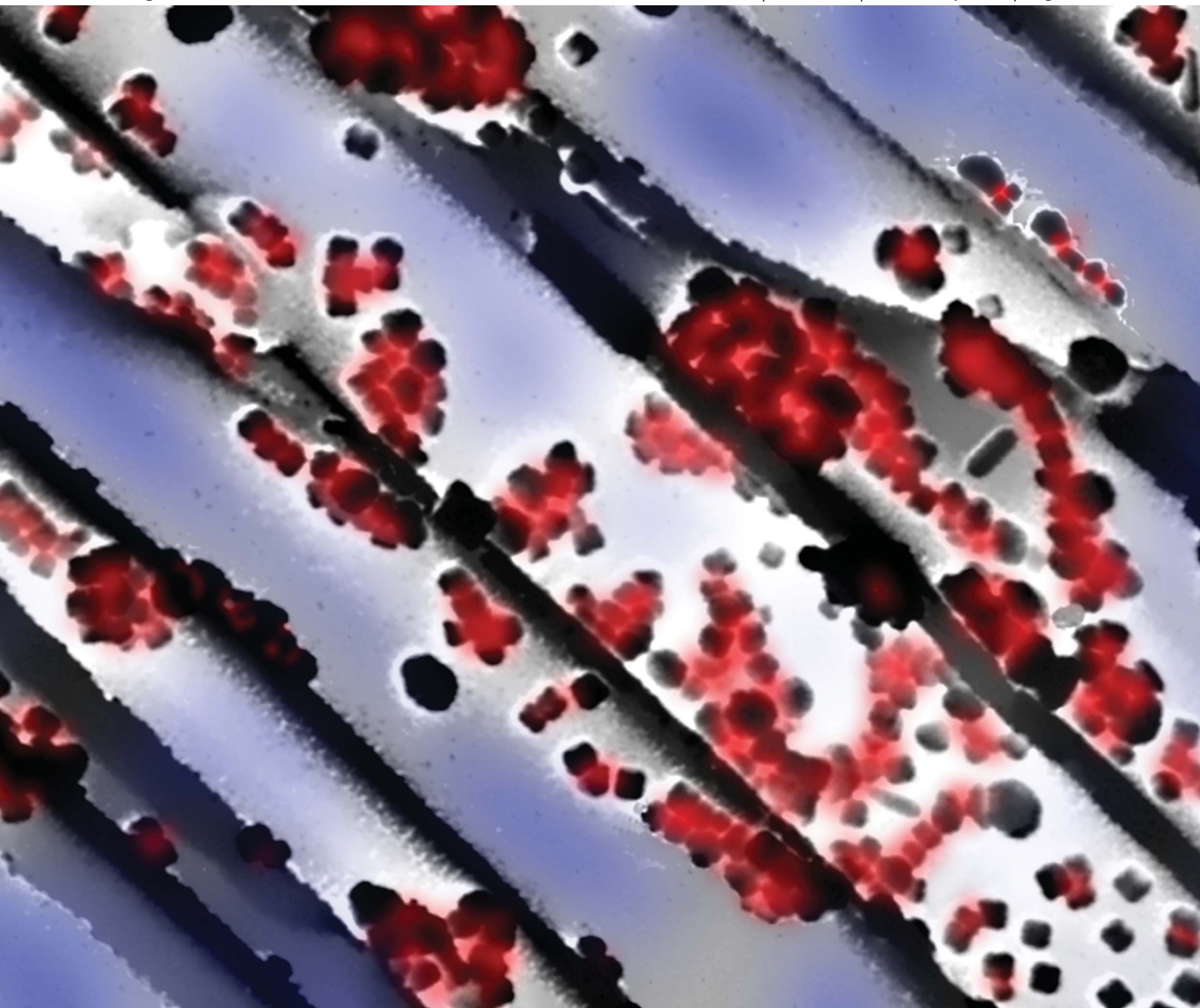


Journal of Materials Chemistry A

Materials for energy and sustainability

www.rsc.org/MaterialsA

Volume 1 | Number 8 | 28 February 2013 | Pages 2677–2928



ISSN 2050-7488

RSC Publishing

PAPER

Vladimir V. Tsukruk *et al.*

Assemblies of silver nanocubes for highly sensitive SERS chemical vapor detection



2050-7488(2013)1:8;1-X

Assemblies of silver nanocubes for highly sensitive SERS chemical vapor detection†

Cite this: *J. Mater. Chem. A*, 2013, **1**, 2777

Rajesh Kodiyath,^{‡a} Sidney T. Malak,^{‡a} Zachary A. Combs,^a Tobias Koenig,^a Mahmoud A. Mahmoud,^b Mostafa A. El-Sayed^b and Vladimir V. Tsukruk^{*a}

We suggest that silver nanocube (AgNC) aggregates within cylindrical pores (PAM–AgNC) can be employed as efficient nanostructures for highly efficient, robust, tunable, and reusable surface-enhanced Raman scattering (SERS) substrates for trace level organic vapor detection which is a challenging task in chemical detection. We demonstrate the ability to tune both the detection limit and the onset of signal saturation of the substrate by switching the adsorption behavior of AgNCs between highly aggregated and more disperse by varying the number of adsorption-mediating polyelectrolyte bilayers on the pore walls of the membrane. The different AgNC distributions show large differences in the trace vapor detection limit of the common Raman marker benzenethiol (BT) and a widely used explosive binder *N*-methyl-4-nitroaniline (MNA), demonstrating the importance of the large electromagnetic field enhancement associated with AgNC coupling. The SERS substrate with highly aggregated AgNCs within the cylindrical pores allows for consistent trace detection of mid ppb (~500) for BT analyte, and a record limit of detection of low ppb (~3) for MNA vapors with an estimated achievable limit of detection of approximately 600 ppt. The dispersed AgNC aggregates do not saturate at higher ppb concentrations, providing an avenue to distinguish between higher ppb concentrations and increase the effective range of the SERS substrate design. A comparison between the AgNC substrate and an electroless deposition substrate with silver quasi-nanospheres (PAM–AgNS) also demonstrates a higher SERS activity, and better detection limit, by the nanocube aggregates. This is supported by FDTD electromagnetic simulations that suggest that the higher integrated electromagnetic field intensity of the hot spots and the large specific interfacial areas impart greatly improved SERS for the AgNCs. Moreover, we demonstrated that the AgNC substrate can be reused multiple times without significant loss of SERS activity which opens up new avenues for in-field monitoring.

Received 28th October 2012
Accepted 13th December 2012

DOI: 10.1039/c2ta00867j

www.rsc.org/MaterialsA

Introduction

The surface-enhanced Raman scattering (SERS) technique is highly sensitive, non-destructive, exhibits high-specificity and recognition for trace-level detection of hazardous chemicals and biomolecules,¹ has levels of detection down to a single molecule,^{2–6} and works at typical environmental temperatures and pressures. Raman enhancement is largely due to the huge electromagnetic field that exists in the small gaps between plasmonic metal nanostructures, termed hot spots.⁷ The increase of the electromagnetic (EM) plasmon field in the gap

between nanoparticles is a result of plasmon field coupling, and leads to the enhancement of the Raman signals from molecules present in the plasmon field domain.⁸ The intensity of the EM field depends on nanoparticle size, shape, curvature of the corners and edges, and the interparticle spacing of aggregates.^{9,10} The EM enhancement factor has been estimated in the hot spot formed between dimers of spherical nanoparticles as well as nanostructures with sharp edges.^{11–14} It has been reported that nanostructures with sharp edges show higher SERS activity than that of spherical nanoparticles due to the presence of greater electric fields at the edges caused by charge concentration.^{15–17}

The most critical aspect for a sensitive and reliable SERS-based detection probe is therefore the design and assembly of well-defined nanostructures with a dense and widespread distribution of particle aggregates (hot spots).¹⁸ Nanocubes (NC) are used for the fabrication of SERS substrates because they have sharp edges with high electromagnetic fields and because they can be synthesized in large quantities with high monodispersity.^{13,15} Moreover, the adsorption of analyte molecules on

^aSchool of Materials Science and Engineering, Georgia Institute of Technology, Atlanta, Georgia 30332-0245, USA. E-mail: vladimir@mse.gatech.edu

^bLaser Dynamics Laboratory, School of Chemistry and Biochemistry, Georgia Institute of Technology, Atlanta, Georgia 30332-0400, USA

† Electronic supplementary information (ESI) available: DFT simulations, AgNC size distribution, additional SEM micrographs, confocal Raman surface scan, weighted linear fitting for LoD, and further detailed explanation of vapor concentrations determination. See DOI: 10.1039/c2ta00867j

‡ These two authors contributed equally to this work.

the surface is favored due to the presence of exposed (001) uniform crystal planes.¹⁶ A number of studies have reported on the SERS activity of silver nanostructures (nanospheres and nanocubes) and their dimers in two-dimensional (2D) substrates and the dependence of their SERS response on the polarization of the excitation light.^{11,13,19–21} Although some of these studies demonstrate impressive limits of detection for AgNCs, most of them have concentrated on the detection of analytes in/deposited from the solution phase^{22,23} or require patterned substrates,²⁴ while the few that performed trace detection over a variety of concentrations concentrated on aqueous phase exposure.²⁵ However, the utilization AgNCs in more complex configurations that can be used in a realistic environment is largely absent and trace level detection over a wide concentration range, and for the vapor phase, has not been performed. SERS substrates based upon open porous alumina membranes (PAM) offer a route to investigate these avenues because they show high SERS activity since the PAM provides a large nanostructure loading capacity, an increased surface area (number of binding sites) for probing molecules, and good transparency and optical wave guiding properties.^{26,27} PAM-based 3D SERS substrates decorated with spherical metal nanospheres have demonstrated effective label-free detection of plastic explosive materials and other small molecules deposited from the liquid phase.^{28–30,34,35}

SERS detection in the vapor phase is still challenging, as demonstrated by the limited number of reports on SERS-based vapor phase detection due to the extremely low concentration of non-volatile analytes.^{31,32} Various design strategies have been developed to fabricate SERS substrates with high SERS activity for liquid phase detection.^{33–37} The few reports demonstrating vapor-phase detection of explosive molecules generally concentrate on planar substrates with a limited number of 'hot spots' in the excitation volume. These can require high laser power (100–115 mW) and long detection time (30 seconds) for collecting spectra thus leading to potential burning of organic analytes.^{38,39} Due to the absence of flow channels in 2D substrates a stream of flowing vapor often must be used which is cumbersome and time consuming.

Although detection studies have investigated nitroaniline molecules,^{40–42} none of these were for vapor phase detection, used AgNCs, implemented 3D substrates, or specifically examined *N*-methyl-4-nitroaniline (MNA). Typically most vapor detection studies have focused on the recognition of the explosive component, such as 2,4,6-trinitrotoluene (TNT) or its byproduct 2,4-dinitrotoluene (DNT),^{43–45} but have not considered common components of munitions such as stabilizing agents like MNA. As known, over the past 20 years the military has moved toward developing insensitive munitions (IM), *i.e.* munitions that are less likely to accidentally explode because they are more resistant to heat and mechanical shock,^{46,47} and in some cases have replaced traditional compounds like TNT because of its shock instability.^{48,49} Therefore, developing sensing platforms that identify stabilizing agents like MNA that are commonly incorporated into the IM compound^{50–52} provides a promising avenue to detect many current and future explosive materials. In addition, MNA has been investigated because it is

an important ingredient in Amatol 40 which is included in the warhead of the V-1 rocket^{53,54} and because it is used as a common additive in explosive materials to depress the melting point in the typical melt-cast process.⁵⁵ However, detection of MNA in the vapor phase is hampered by its low vapor pressure (3×10^{-8} atm).⁵⁶ Therefore, highly sensitive and reliable trace level detection of MNA in the vapor phase requires a SERS substrate that incorporates a large number of SERS hot spots that are densely and consistently distributed throughout the system and accessible to probing molecules.

Herein, we demonstrate that AgNC assemblies can be exploited as efficient nanostructures for SERS-based trace-level vapor detection, allowing for the detection of a common Raman marker benzenethiol (BT) and an explosive-binder (MNA) in the vapor phase down to an unprecedented low ppb–ppt level. In addition, it is shown that AgNCs can be assembled differently within a porous membrane (large aggregates or more dispersed smaller aggregates) depending on the number of polyelectrolyte bilayers that are incorporated onto the pore walls (Fig. 1). This difference in particle adsorption behavior not only leads to noticeable differences in limits of vapor detection but also in saturation onset. The ability to tune the onset of SERS intensity saturation is shown to be an important consideration when designing a SERS substrate because it allows for the proper selection of AgNC adsorption behavior according to the

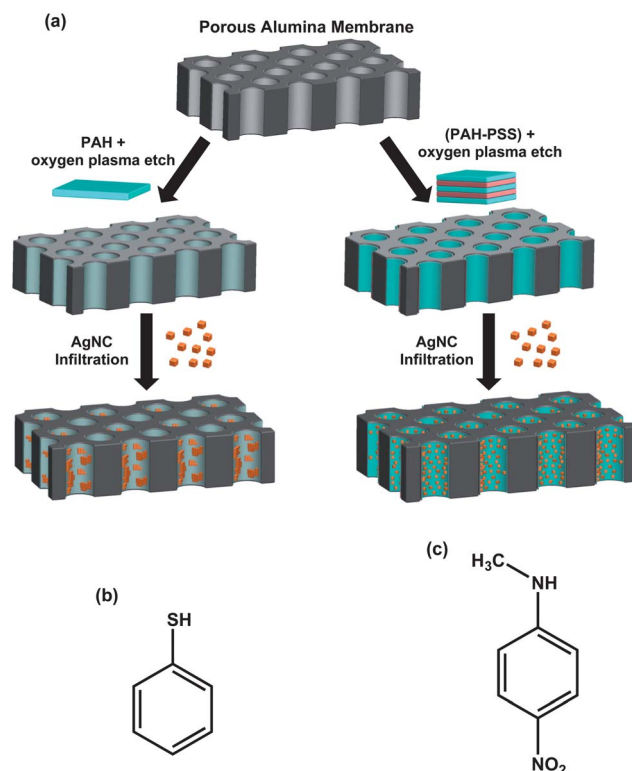


Fig. 1 (a) Schematic of the AgNCs infiltration method showing the porous alumina membrane coated with a positively charged polyelectrolyte (PAH, PEI, or the PAH-PSS bilayers) that is subsequently decorated with silver nanocubes by infiltration. Molecular structures of the two target molecules: (b) the common Raman marker benzenethiol (BT) and (c) the widely used explosive binder *N*-methyl-4-nitroaniline (MNA).

expected concentration range of the analyte that is being detected, providing a potential means for quantitative determination of vapor concentration in real-life situations for specific concentration ranges. The silver quasi-spherical nanoparticles (AgNS) are included in this study as a reference to investigate the effect of nanostructure type and substrate design on SERS activity.^{34,57} The SERS activity of the PAM–AgNCs was found to be much higher than that exhibited by traditional PAM–AgNS, showing very low observed detection limits (LoD) of mid ppb-level (~ 500) for BT, and low ppb-level (~ 3) for MNA vapor concentrations with an estimated ultimate limit of detection of about 600 ppt. The substrate's ability to maintain its detection effectiveness after multiple cleaning and reloading cycles has also been demonstrated and compared to the AgNS substrate, demonstrating an additional consideration when designing robust substrates.

Experimental

Silver nanocube synthesis

AgNCs with an edge length of 40 nm were synthesized using a polyol method as described elsewhere.^{20,58} Briefly, in a 100 mL round bottom glass flask, 70 mL of ethylene glycol (EG) was heated to 150 °C for 1 h. Then a solution of 0.85 g polyvinylpyrrolidone (PVP) dissolved in 10 mL EG was added to the hot EG. 0.4 mL of Na₂S (3 mM) dissolved in EG and 6 mL of 282 mM silver nitrate dissolved in EG were injected, respectively, into the reaction mixture. The reaction mixture was stirred at 200 rpm and refluxed at 150 °C for 10 minutes until the solution became opaque. In order to purify the AgNCs, 5 mL of the prepared AgNC solution was diluted with water and centrifuged at 10 000 rpm for 5 minutes. The precipitated AgNCs were then re-dispersed in water.

PAM–AgNC SERS substrate

PAMs (Anodisc 47, Whatman) were decorated with AgNCs by infiltrating AgNCs suspended in water (AgNC solution) through surface-modified PAMs with a diameter of 47 mm, cylindrical pore diameter of 243 ± 20 nm, wall thickness of 40 nm, and total thickness (depth) of 60 μ m. The immobilization of nanocubes on porous alumina membranes was done using a modified literature procedure.^{59,60} Briefly, the inner surface of the pore walls was modified with a polyelectrolyte to electrostatically assemble the AgNCs onto the pore walls (Fig. 1).⁶¹ The inner surface of the porous membranes was modified with poly(allylamine hydrochloride) (PAH) ($M_w = 58\ 000$; Sigma-Aldrich), polyethylenimine (PEI) ($M_w = 70\ 000$; Polysciences), or poly(sodium 4-styrenesulfonate) (PSS) ($M_w = 70\ 000$; Sigma-Aldrich) by spin-coating (3000 rpm, ~ 45 s) 0.2% aqueous solution followed by rinsing with Nanopure water (18.2 M Ω cm). For the AgNC–PAH and AgNC–PEI substrates 1 layer of the positively charged polyelectrolytes PAH and PEI, respectively, was spin coated onto each side of the PAM (with washing steps before and after polymer deposition). For the AgNC–(PAH–PSS) substrate, 2.5 (PAH–PSS) bilayers were spin coated onto each side of the PAM with washing steps before and after each

polymer deposition. This procedure results in nanometer (2–5 nm) thick polymer coatings depending on the number of bilayers deposited that have been determined by AFM measurements discussed previously.⁶² The surface-modified PAM was then oxygen plasma etched for approximately 5 minutes and then washed to remove the polymer adsorbed on the PAM surface. This treatment minimized adsorption of AgNCs on the PAM surface (and clogging of its pores) during the vacuum infiltration process, allowing for high loading of AgNCs within the pores. The pressure was maintained at 600–700 mmHg during the vacuum infiltration process to ensure wide spread deposition of AgNCs onto the pore walls. Substrates were sonicated and washed after vacuum infiltration to remove excess polymer and AgNCs (Fig. 1).

PAM–AgNS SERS substrate

AgNS were grown on the pore walls following a two-step electroless deposition process.^{29,56} In the first step, the PAMs were immersed in an aqueous solution of SnCl₂ (0.02 M) and HCl (0.02 M) for 2 minutes to deposit Sn²⁺ on the pore walls. The PAMs were then rinsed with Nanopure water and subsequently with acetone and then dried. Growth of silver seeds on the pore walls was carried out in the second step by immersing the PAMs in a 0.02 M aqueous solution of AgNO₃ for 2 minutes followed by a second washing step. The deposition of AgNS seeds was carried out three times to obtain uniform and dense particle coverage on the pore walls. The PAMs with silver seeds were then immersed in 0.5 mL of 10 mM AgNO₃ and 1 mL of 100 mM ascorbic acid for 28 minutes with shaking at 200 rpm. Afterward, the PAMs were removed from the solution, rinsed thoroughly with Nanopure water, and then dried using nitrogen gas. A detailed growth mechanism and time dependence of particle size and distribution using this method have been reported elsewhere.^{56,63}

Characterization

Substrates were characterized using Hitachi-3400 and Zeiss Ultra60 Scanning Electron Microscopes (SEM) at an operating voltage of 5–10 keV. The UV-vis absorption spectra of the SERS substrates were collected using a CraicQDI 202 microspectrophotometer attached to a Leica DM 4000M microscope. Transmission electron microscopy images of silver nanostructures were recorded using a FEI Tecnai F30 TEM with an operating voltage of 300 kV and a JEOL 100CX operated at 100 kV. The TEM samples for AgNS were prepared by dissolving the SERS substrate in 0.1 M NaOH solution and then putting them through dialysis to isolate the nanostructures. The resulting solution was drop cast onto a formvar carbon coated TEM grid.

SERS vapor detection

The vapor-phase detection setup is shown in Fig. 2. The suspended substrate was kept ~ 3 cm above the bottom of the vial. The concentration of BT in the vapor phase was controlled and varied by evaporating known amounts of BT from solution (in ethanol) at 45 °C for 4 hours. MNA vapor was produced by heating approximately 15 mg of solid MNA (melting point = 150 °C)⁶⁴ for 2 hours to ensure saturated MNA vapor conditions. A water bath

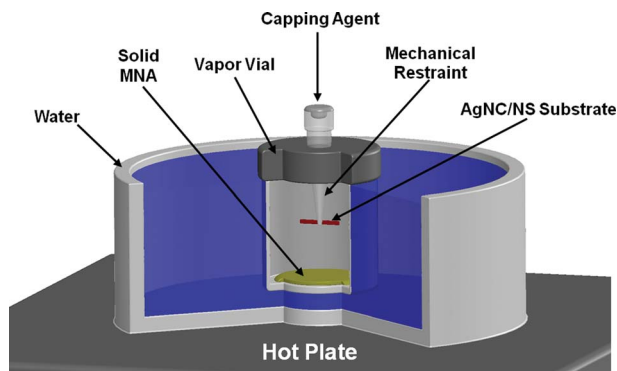


Fig. 2 Experimental setup used for the vapor-phase detection. The substrate is suspended above the solid form of the target substance. The containment vial is heated at various temperatures to produce different vapor concentrations of the target substance. A water bath is used to minimize radial and axial temperature gradients within the vial.

was used to heat the vial to minimize radial and axial temperature gradients throughout the vial volume. The temperature was monitored and automatically adjusted by a thermocouple and maintained to within 0.5 °C of the specified temperature. The experimental setup restricted complete submersion of the glass vial in the water bath so a thermocouple was used to determine the relationship between the water bath temperature and the vial's internal gas temperature. The vapor concentration of MNA in the vial was controlled by changing the vapor pressure of MNA by adjusting the internal temperature of the vial. A more detailed discussion of the calculation of MNA vapor concentration is provided in the ESI.† The experimental setup adopted in this study was chosen because it mimics simple gas diffusion behavior which more closely resembles potential real-world environments (warfield arena, cargo holds, *etc.*) than other flow-based setups that utilize a targeted puff of analyte vapor or constant pumped vapor flow through the substrate to mimic analyte presence.⁶⁵

To demonstrate the reusability of our substrates, we adopted a solvent washing method to remove the adsorbed MNA molecules from the nanoparticle surfaces. The PAM–AgNC and PAM–AgNS substrates were loaded with MNA, submerged in ethanol for 2 min followed by rinsing in excess of ethanol, and then air dried. This was repeated multiple times to test the robustness of the substrate's SERS response to washing–exposure cycles.

The Raman measurements were performed using a WiTec confocal Raman microscope (Alpha 300R) with an Ar⁺ ion laser of wavelength 514 nm and a power of 50 μW according to the usual procedure adapted in our laboratory.⁶⁶ At least 5 spectra, each with a 10 s exposure time, were collected and averaged to ensure accurate results. Mapping images were acquired with a lateral resolution of about 300 nm and a vertical resolution of about 1 μm with a 50× objective lens (spot size diameter ≈ 830 nm).

Density functional theory (DFT) simulation of the SERS spectra of MNA

The MNA molecule was optimized at the B3LYP/6-31++G** level of theory using the quantum chemistry package Gaussian 03.⁶⁷

The geometries of the complex systems, *i.e.* MNA bound to a 2 atom silver cluster (Fig. S1†) were optimized at the B3LYP/LANL2DZ level of theory for the Ag atoms and at the B3LYP/6-31++G** level for the atoms of MNA to estimate the different vibrational modes of MNA molecule.

Finite-difference time-domain (FDTD) simulations

The FDTD method was used to calculate the extinction spectra and the plasmon field enhancement of AgNCs and AgNS (using the commercial software from Lumerical Solutions Inc. FDTD Solutions, Version 7.5.7).^{68–70} Nanocubes coated with a PVP-layer and different edge rounding values were used to explain the extinction observed experimentally. Edge rounding is defined as R/L where L is the nanocube edge length and R is either the radius of a cylinder fitted to a rounded edge or of a sphere fitting to a rounded corner, as established in the literature.⁷¹ The PVP-layer and the nanocube were defined by the same edge rounding factor.

The PVP-layer was specified with a permittivity of 2.25 while silver was specified with a wavelength dependent permittivity from CRC.⁷² Fit analysis at the CRC source showed an RMS error of 0.045 by 6th order polynomial. The permittivity of water was taken from Palik (first order fit with an RMS error of 0.029).⁷³ The simulation mesh size was chosen to be 0.5 nm for the best possible rendering of edge rounding and second conformal variant for mesh refinement. Anti-symmetric and symmetric boundary conditions were used to reduce the simulation time.

Results and discussion

Fig. 3a displays TEM images of the AgNCs used in this study with a narrow size distribution, an edge length of 40 ± 3 nm (see Fig. S3† for particle distribution), and an interparticle face–face spacing of 1.8 ± 0.8 nm. The quasi-spherical silver nanoparticles have an average diameter of 30 ± 10 nm (Fig. 3b).

Zeta potential measurements of the AgNC solution show that PVP-capped AgNCs possess a strong negative surface charge (−40 mV, pH 5.0), which should provide a strong attraction to the pore walls that are coated with positively charged PAH or PEI.^{28,34,35} Analysis of the SEM images of the PAH, PEI, and (PAH–PSS)-coated substrates in Fig. 4a, b, and c (respectively) shows a dense distribution of AgNCs over several microns depth from the top surface of the PAM. Both PAH and PEI were utilized to fabricate substrates to demonstrate that the fabrication of these substrates does not require a specific positively charged polyelectrolyte. Fig. 4d is an SEM image of the PAM–AgNS fabricated by the electroless deposition method, showing a uniform deposition of quasi-spherical nanoparticles over the entire PAM.^{29,30}

The high adsorption of particle density of AgNCs on the pore walls is due to the strong electrostatic attraction between the positively charged polyelectrolyte layer and the negatively charged PVP-coated AgNCs. The majority of AgNCs in the PAH and PEI substrates are assembled in many-particle densely packed aggregates (see Fig. S4†), which leads to enhancements in the SERS response through the presence of SERS hot spots

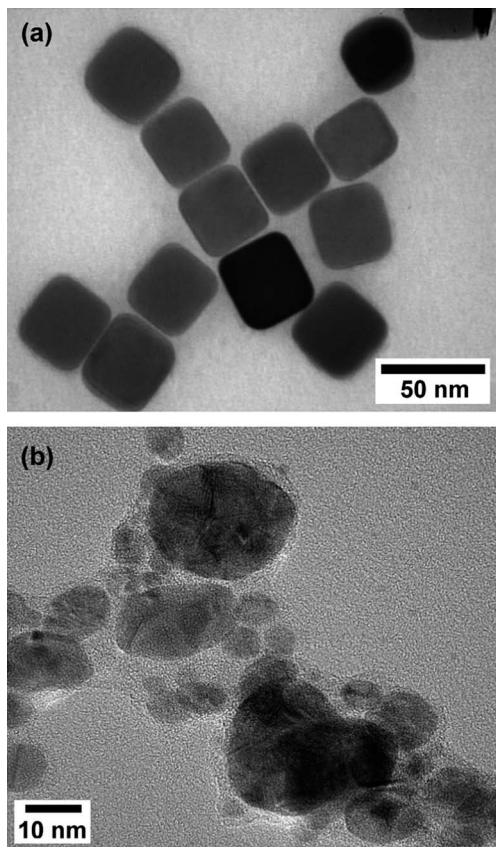


Fig. 3 TEM micrographs of (a) Ag nanocubes capped with a PVP stabilizing layer that were synthesized using a polyol method and (b) silver quasi-nanospheres grown on a PAM using an electroless deposition method which were subsequently released by dissolution of the PAM by NaOH.

between closely adjacent nanocubes. The AgNC-(PAH-PSS)_{2.5} substrate on the average demonstrates single and smaller AgNC aggregates that are more dispersed than the PAH and PEI

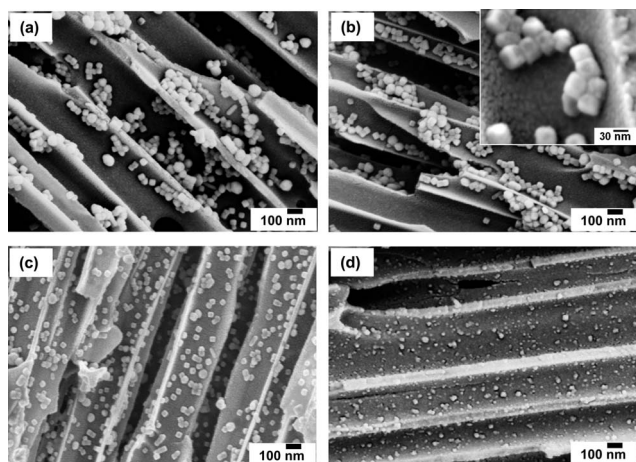


Fig. 4 SEM images of the cross-section of the infiltrated substrates (a) PAM-AgNC (PAH), (b) PAM-AgNC (PEI), and (c) PAM-AgNC (PAH-PSS)_{2.5} demonstrating a very high particle adsorption density; the inset shows higher magnification. (d) SEM image of the cross-section of the PAM-AgNS substrate produced *via* the electroless deposition method. The PAM-AgNC (PAH-PSS)_{2.5} and PAM-AgNS substrates demonstrate more evenly dispersed nanostructures.

substrates (see Fig. S5† for more images). This difference in adsorption behavior is likely due to the PAH and PEI substrates not having as uniform a polymer layer over the pore surface area after the oxygen plasma etching process, while the (PAH-PSS)_{2.5} substrate has multiple bilayers that are electrostatically bound which are more resistant to oxygen plasma etching. The presence of aggregates can be explained by the shielding of the repulsive electrostatic interaction between PVP-capped AgNCs by the highly positive terminating cationic polymer layer (PAH) on the PAM pore walls which minimizes the repulsive electrostatic interaction between adjacent PVP coated AgNCs,^{74,75} potentially allowing for AgNCs to adsorb close to each other *via* van der Waals interactions. In addition, it is evident from Fig. 4a, b, and c that the majority of the AgNC aggregates assemble with a face-to-face orientation which is due to van der Waals attractions having a stronger influence over assembly orientation than steric hindrance between PVP chains of adjacent AgNCs, an expected result for particles stabilized with short-chain polymers.⁷⁶

The face-face contacts can red shift the surface plasmon resonance (SPR) absorption of the AgNCs, which has been observed (Fig. 5).⁷⁰ The SPR absorption at 450 nm is due to dipolar resonance while the higher energy peaks at 390 and 350 nm are attributed to multipolar excitations.⁵⁷ To confirm this, we have simulated the SPR absorption spectrum of a 40 nm AgNC coated with PVP in water using the FDTD method (Fig. 5a).

As is clear from the simulated spectrum, the extinction is clearly dominated by absorption, which is expected for a cube with 40 nm dimensions.⁷⁰ Surface charge distributions show resonances due to the excitation of dipole (I) and higher cube modes (II-IV). The FDTD simulation included a PVP-layer and an edge rounding of the AgNCs to match the FDTD predictions to the experimental results. The edge rounding induces an increase of symmetry of the charge distribution, which reduces the number of resonances.⁷⁷ Consequently, only four excitation modes are observed for the rounded cube as compared to the six excitation modes exhibited by a perfect cube.⁷⁰ The inset in Fig. 5a shows how the presence of the higher refractive index PVP layer (estimated to be 1–2 nm) red shifts the dipole-peak position about 6 nm compared to a perfect cube (indicated as 1 to 2 in the inset) whereas the AgNC SPR absorption blue shifts as the edge rounding increases (indicated as 2 to 3 in the inset). An exact match between the FDTD simulation and the experimental results occurs for an edge rounding factor of 12.5%, which is reasonable considering the multiple treatment steps involved in the substrate preparation and the TEM micrographs (Fig. 3). The lack of an absorption peak in the lower energy region indicates that there is minimal particle aggregation occurring in solution,²⁰ suggesting that aggregation occurs primarily during particle adsorption onto the substrate.

The PAM-AgNC (PAH) and (PEI) substrates show a clear peak at 479 and 502 nm, respectively, and broad absorption between 600 and 800 nm (Fig. 5b). The red shift of the dipole resonance absorption from 450 nm in the solution to 479 and 502 nm in the AgNC substrates (PAH and PEI, respectively) can be attributed to dipole plasmonic coupling of aggregates in the

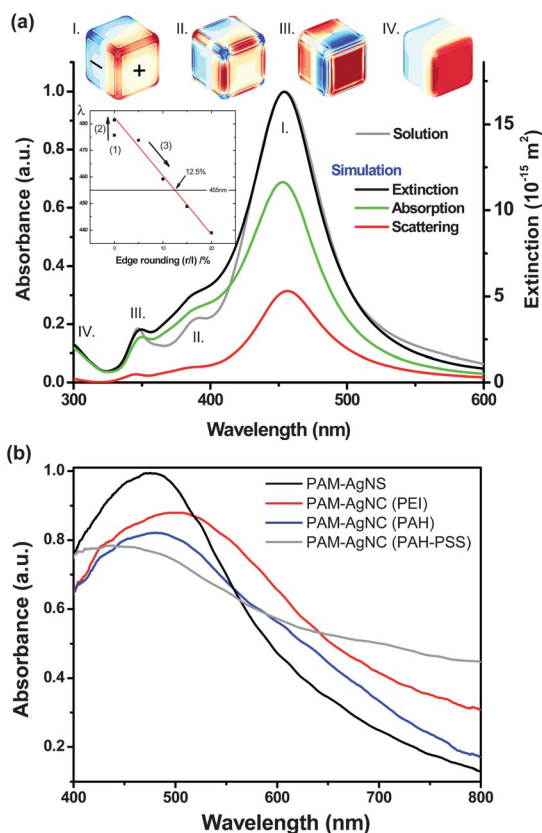


Fig. 5 (a) Simulated FDTD and experimental spectra of 40 nm AgNCs in water (the different modes of oscillation associated with the AgNCs are shown in the top inset). (b) UV-vis absorption spectra of the PAM-AgNC and PAM-AgNS substrates, which all show high absorption at the laser wavelength (514 nm).

substrate.⁵⁷ The broad absorption in the 600–800 nm range could be due to the presence of aggregates with different orientations, sizes, and inter-particle distances, which is observed in the substrate SEM images (Fig. 4a–c).^{20,75} The PAM-AgNC (PAH-PSS)_{2.5} substrate has a strong resonance located at 450 nm, which is similar to the dipole resonance peak of the AgNC solution. This similarity is not surprising since the AgNCs in this substrate are generally more disperse. Fig. 5b also shows the absorption spectrum of PAM-AgNS. The optical absorption for the PAM-AgNS substrate is maximum around 475 nm due to the silver nanoparticle aggregation. In addition, the refractive index of the alumina membrane (1.6) may also contribute to the observed red shift.^{78,79} The increased absorbance of the AgNC substrates (with respect to the AgNS substrate) in the 600–800 nm region indicates a broader distribution in the aggregate resonance frequency. This difference is reasonable since NCs have more orientation parameters that can affect dipole plasmonic coupling of aggregates due to their shape.

SERS activity from the PAM-based SERS substrates

The fabricated substrates are expected to show a high SERS response since they have considerable absorption at the 514 nm excitation wavelength.⁸⁰ Fig. 6a shows SERS spectra of BT detected in the vapor phase using the PAM-AgNC (PAH) substrate. The characteristic peaks of BT at 1584 cm⁻¹ (C=C)

stretching), 1077 cm⁻¹ (C–C bending) and 999 cm⁻¹ (ring breathing) are observed at different vapor concentrations.⁸¹ Note, there is an overlap of the amorphous carbon peak and the BT peak at 1584 cm⁻¹, making it difficult to use this peak for reliable detection. However, the other two characteristic peaks from BT (999 cm⁻¹ and 1077 cm⁻¹) are clearly visible for 500 ppb. From Fig. 6a it can be concluded that a BT vapor concentration of 500 ppb can easily be detected with our SERS substrates. A clear difference in the SERS intensity of the peak 1077 or 999 cm⁻¹ was not observed with concentration. This may be due to the fact that the detectable concentration of BT in this study (500 ppm) is sufficient to form a monolayer of BT on the nanoparticle surface, which means additional increases in BT concentration will not significantly affect the SERS response due to the highly localized nature of the hot spot region. The LoD we achieved with our SERS substrate is one order of magnitude lower than that reported for BT.⁸² This low LoD for BT demonstrates the high SERS activity of our substrates and suggests that they will be an effective detection platform for MNA.

The SERS substrates were exposed to six different MNA vapor concentrations that were established using specific temperatures: 3 ppb (5 °C), 10 ppb (15 °C), 29 ppb (25 °C), 99 ppb (35 °C), 297 ppb (45 °C) and 790 ppb (55 °C),⁵⁵ a procedure similar to previous studies.⁶³ The ppb vapor concentration of MNA was estimated using theoretical calculations of the MNA vapor pressure at different temperatures and by assuming ideal gas conditions (applicable given the low pressure and temperatures involved), as is standard practice for parts per vapor concentration estimations (see the ESI†).⁵⁵

The simulated MNA molecule spectrum shows a strong peak at 1363 cm⁻¹ and several other peaks at 865, 1133, and 1655 cm⁻¹ (Fig. S1†). Modeling suggests that the peaks at 1363 cm⁻¹ and 865 cm⁻¹, although shifted, may be due to symmetrical stretching and out-of-plane bending of the –NO₂ group, respectively.³⁵ The peaks at 1133 and 1655 cm⁻¹ arise from C–H in-plane bending and stretching of the aromatic ring, respectively.⁸³ To understand the effect of binding of the analyte molecule to silver, we simulated the SERS spectrum of MNA using a two-atom silver cluster which shows selective peak enhancement which is consistent with experimental results (Fig. 6, S1†).³⁰

The SERS spectra of MNA from the vapor phase with two different substrates, PAM-AgNCs and PAM-AgNS, are shown in Fig. 6. Note that the clean, unexposed substrates (denoted REF in each plot) show no coherent peaks at the 857 or 1157 cm⁻¹ position. During spectra acquisition the laser power is attenuated to 50 μW (nearly three orders of magnitude lower than that usually reported) to minimize undesirable phenomena such as photobleaching and photodesorption.⁸⁴ The characteristic Raman peaks of MNA at 857, 1157, 1300, and 1620 cm⁻¹ are clearly observed for different concentrations of MNA vapor. The spectral positions of the characteristic vibrational modes are shifted slightly in the SERS spectra with respect to the Raman spectra of pure MNA (Fig. S2†) and the simulated MNA SERS spectra. This minor spectral shift could be due to metal-analyte interactions at the nanoparticle surface and due to the presence

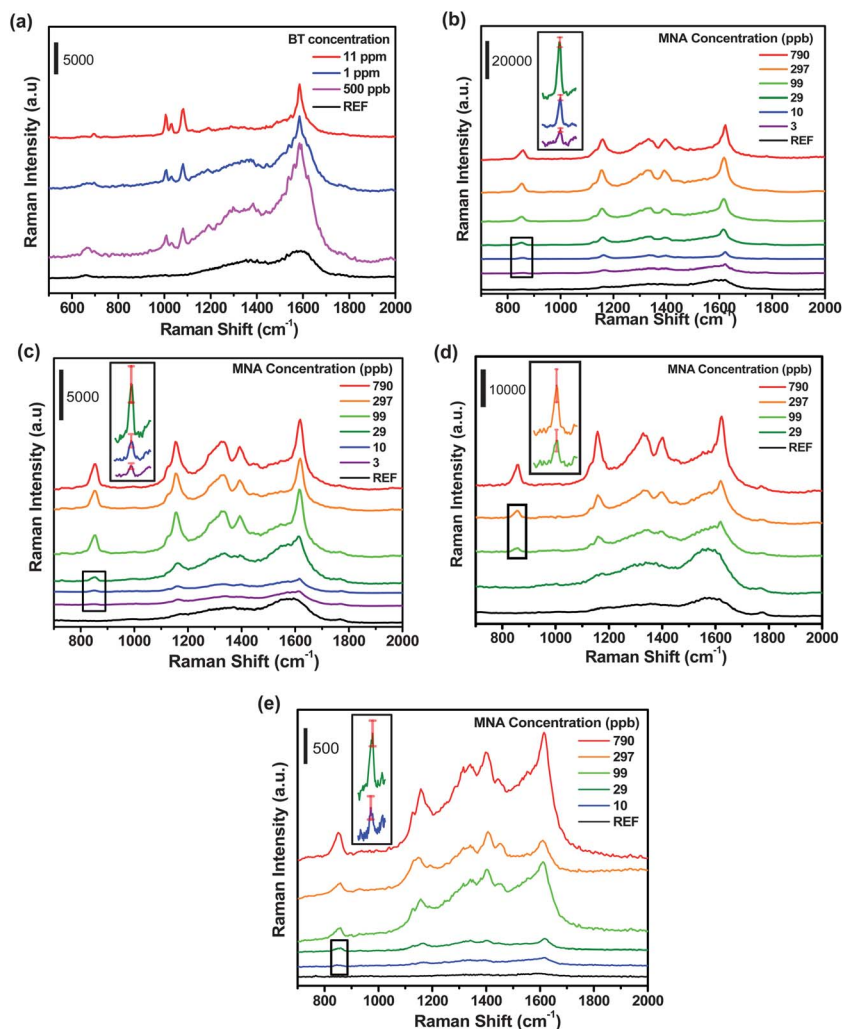


Fig. 6 SERS spectra of (a) BT vapor by PAM-AgNC (PAH), and MNA vapor by (b) PAM-AgNC (PAH), (c) PAM-AgNC (PEI), (d) PAM-AgNC (PAH-PSS)_{2.5}, and (e) PAM-AgNS substrates at various vapor concentrations. The REF for each plot is the bare substrate (*i.e.* no exposure to MNA). The SERS spectra were vertically translated for clarity. The insets display the 857 cm⁻¹ peak at the lower concentrations, where the error bars represent the standard deviation of the peak height (the scale bars do not apply to the insets).

of PVP on the nanoparticle surface which may induce steric hindrance to the adsorbed MNA molecules.

It is important to note that the Raman band at ~ 1620 cm⁻¹ is enhanced greatly compared to the bulk MNA spectrum which suggests that the MNA molecule adopts a 'face-on' conformation to the metal nanoparticles.⁸² Fig. 6 shows that the SERS activity of PAM-AgNC (PAH) was found to be more than an order of magnitude higher than that observed for the PAM-AgNS substrates for the 857 and 1157 cm⁻¹ peaks for all concentrations. The PAM-AgNC (PAH-PSS) and PAM-AgNC (PEI) substrates showed a response similar to the PAH-substrate, although reduced slightly at most concentrations. The inset of each plot in Fig. 6 shows the 857 cm⁻¹ peak at lower concentrations, where the error bar represents the standard deviation of the peak height. The insets show that a clear peak is present down to 3 ppb and 30 ppb for the AgNC and AgNS substrates, respectively, if a signal to noise ratio of >3 is considered.

Variation of the Raman intensity of the 857 and 1157 cm⁻¹ peaks with MNA vapor concentration is shown in Fig. 7. This

figure shows that the Raman intensity of the peaks (fitted using a Lorentz function) increases with MNA concentration until they saturate at 300 ppb and 100 ppb for the PAM-AgNC (PAH) and PAM-AgNC (PEI) substrates, respectively. Neither the AgNS nor the AgNC-(PAH-PSS)_{2.5} substrate demonstrates saturation for the concentration range studied. This is likely due to the more dispersed adsorption pattern of the nanostructures in these substrates which leads to a larger effective surface area. Therefore, the AgNC (PAH) and (PEI) substrates are very effective for low ppb detection but are unable to distinguish between higher vapor concentrations, while the AgNC-(PAH-PSS)_{2.5} and AgNS substrates demonstrate the ability to distinguish between higher ppb concentrations. The ability to change the adsorption behavior of AgNCs can therefore offer a means to tailor the substrate's effective concentration response which is an important parameter when designing in-field sensors.

Fig. 7a and b show that MNA vapor concentrations of approximately 3 ppb can be detected easily by the AgNC-(PAH) and (PEI) substrates by identifying either the 857 or 1157 cm⁻¹

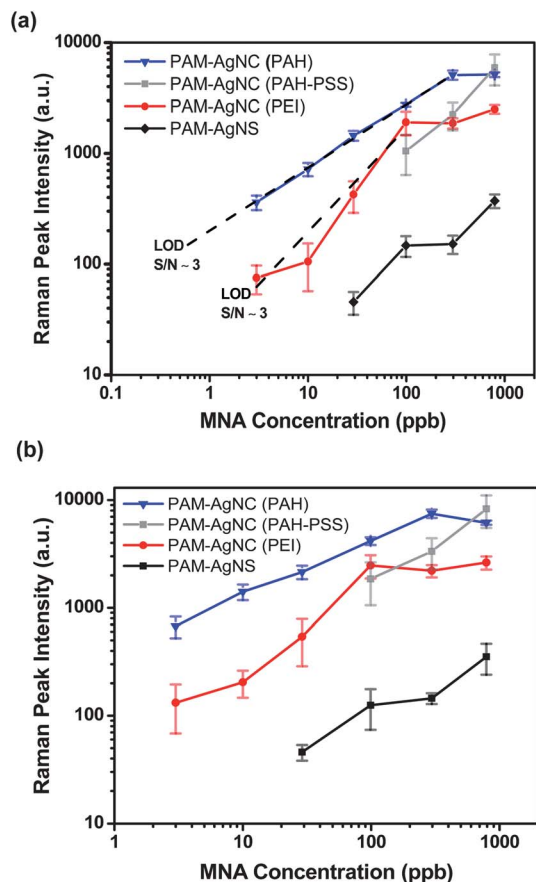


Fig. 7 Variation of the SERS intensity versus concentration between the PAM-AgNC (PAH), PAM-AgNC (PEI), PAM-AgNC (PAH-PSS)_{2.5}, and PAM-AgNS substrates for the (a) 857 cm⁻¹ and (b) 1157 cm⁻¹ peaks. The dashed lines in (a) are linear fits, where the data points are weighted according to the inverse square of their standard deviation, as noted in the text.

peak, where a signal-to-noise ratio of at least 3 was used to identify peaks. This is a record level of detection for MNA in the vapor phase. The PAM-AgNS does show the 857 and 1157 cm⁻¹ peaks at 10 ppb, however, they were not included because the coefficient of variation was 0.43 and 0.85, respectively, making them statistically unreliable. Therefore, the PAM-AgNS is able to reliably detect a concentration of 30 ppb, demonstrating that the detection limit of the PAM-AgNC substrate is one order of magnitude better than that observed for PAM-AgNS substrate. The AgNC-(PAH-PSS)_{2.5} substrate demonstrates detection down to 100 ppb but shows no reliable peak intensity at lower concentrations. This is not surprising since this substrate is dominated by dispersed, individual AgNCs and smaller sized aggregates. However, as mentioned previously it demonstrates a linear response at higher concentrations that may be useful for quantitative determination of vapor concentration in this region (Fig. S6†).

The ultimate theoretical LoD for MNA vapor by the PAM-AgNC (PAH) and (PEI) substrate was determined by applying an instrumental error-weighted linear fit to the 857 cm⁻¹ peak intensity data shown in Fig. 7a and extrapolating to a signal-to-noise ratio of 3 (Fig. S7 and S8†). The instrumental error-weighted linear fit weights each data point according to the

inverse square of its standard deviation ($w_i = 1/(\sigma_i)^2$), and the noise was determined by calculating the standard deviation from a linear fit to a linear region of the reference spectra. The *R*-squared value was significantly improved when the saturated data points were excluded from the fitting (Fig. S7 and S8†). This analysis shows a theoretical limit of detection of approximately 600 ppt and 3 ppb for the AgNC-PAH and AgNC-PEI substrates, respectively, demonstrating a LoD more than an order of magnitude better than the AgNS substrate. The LoD of the PAM-AgNS substrate was not calculated since the standard deviation of the 857 cm⁻¹ peak at 30 ppb already put it at or below the reliable signal-to-noise ratio of 3. The AuNC-(PAH-PSS)_{2.5} substrate demonstrates an observed LoD of approximately 100 ppb so a theoretical LoD was not calculated for it. As mentioned, this decrease in sensitivity compared to the AgNC-PAH and AgNC-PEI substrates is likely due to a decrease in the number of SERS hot spots due to the more dispersed arrangement of AgNCs.

Electromagnetic simulation on AgNC (edge length 40 nm with a PVP layer of 1.5 nm thickness) and AgNS (diameter 40 nm with no PVP layer) dimers separated by various interparticle distances clearly shows that the AgNC dimers have a higher integrated electric field intensity than the AgNS dimers for all interparticle distances (Fig. 8). The dimers were excited with a wavelength of 514 nm with a polarization along the long axis of the dimer (labeled in Fig. 8 as the E-arrow, where the k-arrow indicates the propagation direction). The electric field intensity was integrated over a planar profile located at the half height (labeled as the monitor in the top panel of Fig. 8) at the hot-spot area. The integrated electric field intensity in the hot spot as a function of interparticle distance is shown in Fig. 8c. The field intensity was found to be enhanced 50 times for AgNC dimers compared to that between AgNS for all interparticle separations. The intensity of the cube dimer is always higher compared to the particle dimer because the cube shape leads to more efficient separation of charges and the high curvature corners allow for larger charge concentration.¹⁵⁻¹⁷ In addition, the presence of aggregates in the PAM-AgNCs is higher than that in the PAM-AgNS which suggests more hot spots available for SERS enhancement. Moreover, the AgNC has the (001) plane exposed at the surface while the nanoparticle surface is dominated by the (111) plane. It has been reported that the surface energy of the (001) plane is higher than that of the (111) plane so molecular adsorption is more favorable for the AgNCs and hence SERS activity should increase.^{16,30}

In order to characterize the SERS activity of the 3D PAM-AgNCs, Raman mapping of the characteristic MNA peaks in both the (*x,y*)-plane (substrate surface) and along the *z*-direction (pore depth) of the PAM-AgNC substrate was conducted for the 297 ppb vapor concentration (Fig. 9a and b). The mapping was conducted by monitoring the intensity of the 857 cm⁻¹ peak at different *z*-positions of (*x,y*) scans. The representative 20 μm by 20 μm 2D Raman map shows that there is a relatively uniform SERS response over the entire region, with a coefficient of variation of 11% of the SERS intensity which was found by averaging the 3600 data points over the surface area (approximately 300 nm step sizes). The same surface scan measurement

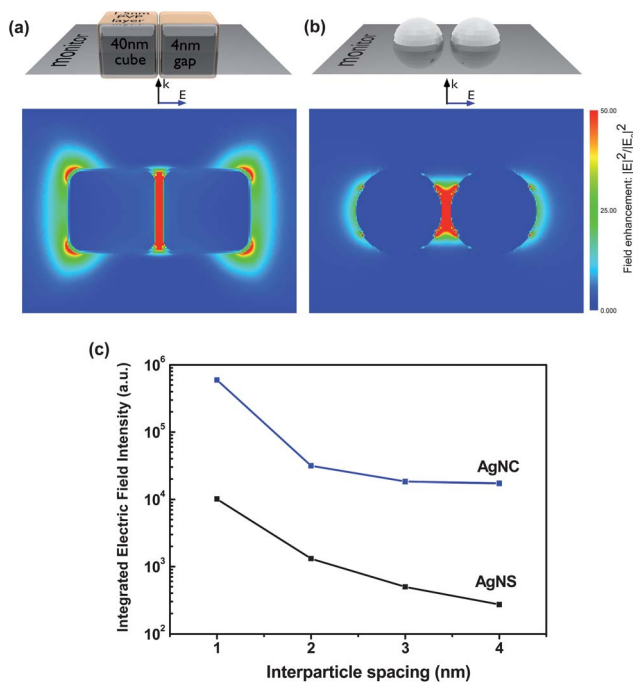


Fig. 8 FDTD simulation of the electric field intensity of the gap between (a) AgNC (with 40 nm edge length) and (b) AgNS (40 nm diameter) dimers. The gap between the nanoparticles is 4 nm. (c) Variation of the planar integrated electric field intensity of the hot-spot as a function of inter-particle separation.

was made for the PAM–AgNC (PAH–PSS)_{2.5} substrate (Fig. S9†) and yielded comparable results. This variation is likely a combination of differences in nanoparticle adsorption due to the macroscopic vacuum infiltration process and the inherent difference in nanoparticle adsorption density between the substrate surface and within the pores. For z-mapping, the SERS activity was mapped by again monitoring the 857 cm⁻¹ peak through the depth of the nanopores. It shows that the largest SERS enhancement occurs within the first 3–6 μm depth beneath the PAM surface region similar to previous reports (Fig. 9b).^{29,30} SERS spectra of MNA obtained at different depths from the top surface of the PAM show the characteristic MNA spectrum (Fig. 9c). The reduction in intensity of the identifying peaks with depth is likely due to a combination of the reduced particle density with pore depth and a decrease in light intensity with pore depth.²⁹ However, the intensity of the 857 cm⁻¹ peak is present throughout the whole region of observed high AgNC density which suggests that the porous nature of the PAM allows MNA molecules to diffuse at least 6 μm into the pores. We suggest that the analyte molecules can access the AgNC surface and get adsorbed. Indeed, the catalytic activity of nanostructures protected with a PVP layer suggests that the surface is not fully covered with the polymer,⁸⁵ and that the analyte molecules can access the AgNC surface. The total SERS activity reported here may be also a cumulative effect obtained from

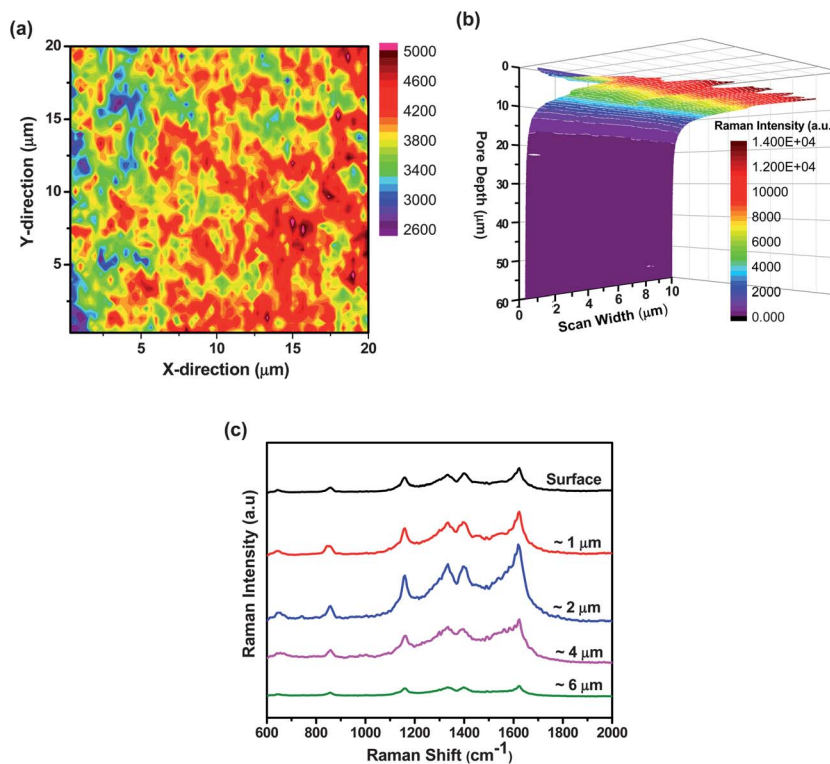


Fig. 9 (a) Confocal Raman surface mapping (20 μm by 20 μm) of the 857 cm⁻¹ peak of MNA for a representative PAM–AgNC SERS substrate. (b) Confocal SERS z-mapping of the 857 cm⁻¹ peak of MNA through the depth of the porous alumina membranes. (c) SERS spectra of MNA at different depths of the PAM–AgNC SERS substrate.

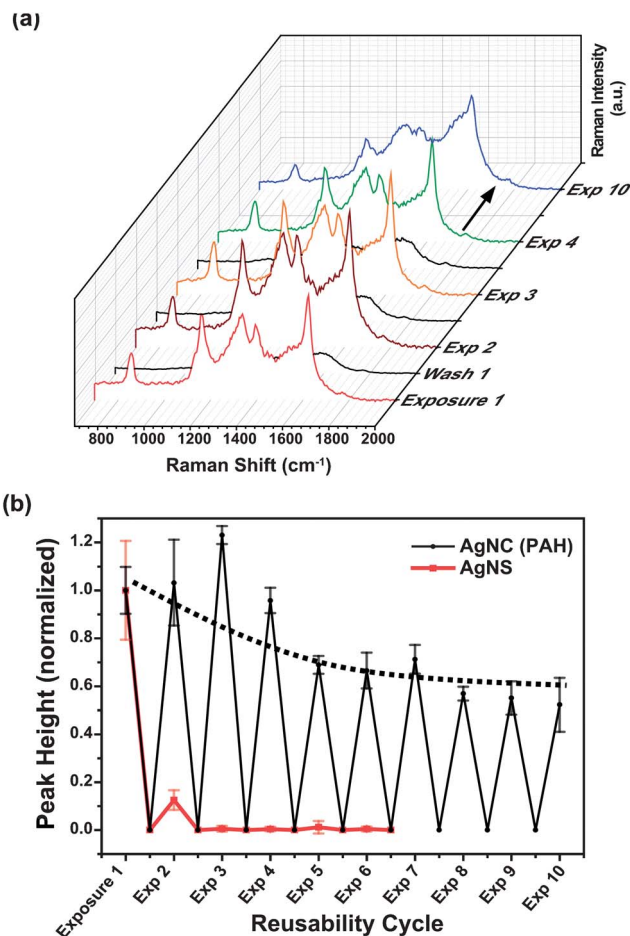


Fig. 10 (a) SERS responses of PAM-AgNCs during repeated MNA exposure–ethanol washing cycles (the sample was exposed to MNA vapor created at 45 °C). (b) The normalized SERS response of the 857 cm⁻¹ peak through multiple exposure–wash cycles (the dotted line is a visual aid). The AgNC (PAH) and AgNS SERS response were normalized according to the intensity of the 857 cm⁻¹ peak from the first MNA exposure for each substrate.

SERS contributions from multiple depths, which is an added advantage for our PAM-based 3D substrates.

The reusability of the substrates was also investigated by exposing the substrates to multiple MNA exposure–ethanol wash cycles. The AgNC substrates were found to be robust against solvent washing and could be readily reloaded for repeated tests, a characteristic that has recently become an important consideration when evaluating the durability of SERS substrates.^{86,87} Fig. 10a shows the SERS response of the substrate which was exposed to MNA at 45 °C after repeated MNA exposure–ethanol washing cycles. The SERS activity of the substrate was monitored by tracking the peak intensity of the 857 cm⁻¹ peak (Fig. 10b). The SERS activity was nearly constant for the first four repeated measurement–washing cycles and then decreased and finally stabilized in the subsequent cycles. The reduction in intensity is likely due to the removal of lightly bound, physically adsorbed AgNCs during the washing steps. This is further supported by the apparent leveling of the SERS intensity (at later washing steps), which likely occurs as the loose AgNCs are removed and the total number of AgNCs approaches a constant

value. A baseline intensity of <2% was observed after each washing step (Fig. 10b). The AgNS substrate was not nearly as robust against ethanol washing, showing approximately an 85% decrease from its initial intensity after only one ethanol washing, with subsequent cycles showing a decrease in the intensity to nearly zero. This decrease is likely due to a combination of AgNS removal and oxidation, which has been shown to drastically reduce the SERS activity of AgNS.⁸⁸ The difference between the AgNC and AgNS substrates in response to washing is likely due to the presence of the PVP capping layer on the AgNCs which minimizes degradation of the AgNCs by ethanol, whereas the AgNS have no protective polymer capping layer.

Conclusions

In conclusion, we have demonstrated that AgNC aggregates act as efficient nanostructures for trace level vapor detection of the common Raman marker BT and the explosive binder MNA. The high electric field, large surface area, and large hot-spot volume associated with the nanocube–nanocube contacts are efficiently utilized in combination with the enhancement effects provided by PAMs to develop highly active, robust, and reproducible SERS substrates for trace level detection with record sensitivities. A method for varying the adsorption dispersion of AgNCs on the PAM pore walls from large aggregates to dispersed AgNCs demonstrated the importance of aggregates on SERS effectiveness (by hot spot formation) and also a method to increase the effective range of AgNC substrates by changing the onset of saturation. FDTD simulations support the suggestion that the higher SERS activity of the AgNC substrates, compared to the AgNS substrate, is in part due to a combination of higher electric field intensity in gaps and nanocube dimer coupling. The exploration of silver nanocube aggregates on porous substrates shows high SERS activity in the vapor phase with a record detection level for BT and MNA (500 ppb and 3 ppb respectively). To the best of our knowledge, this is the first report on the *trace detection of MNA* in the vapor phase.

In addition, the AgNC substrates were found to be reusable, demonstrating a consistent SERS activity after multiple exposure–wash cycles. Reusability has therefore become an important design parameter for evaluating the usefulness of SERS detection systems and will likely promote the acceptance of SERS as an in-field analytical tool in the areas of life sciences, medical evaluation, and defense. Our results indicate that SERS has the potential to be employed as an effective, reliable detection platform for common explosive stabilizers in the vapor phase over a wide concentration range.

Acknowledgements

Financial support from the DARPA/US Army W31P4Q10C0027 grant through EngeniusMicro and NSF-CBET (SERS measurements), and from the U.S. Department of Energy, Office of Basic Energy Sciences, Division of Materials Sciences and Engineering under Award # DE-FG02-09ER46604 (silver nanocube synthesis and simulations) is gratefully acknowledged. Z. A. Combs thanks the support under and awarded by DoD, Air

Force Office of Scientific Research, National Defense Science and Engineering Graduate (NDSEG) Fellowship, 32 CFR 168a.

References

- Z. A. Combs, S. Chang, T. Clark, S. Singamaneni, K. D. Anderson and V. V. Tsukruk, *Langmuir*, 2011, **27**, 3198–3205.
- S. M. Nie and S. R. Emery, *Science*, 1997, **275**, 1102–1106.
- K. Kneipp, Y. Wang, H. Kneipp, L. T. Perelman, I. Itskan, R. Dasari and M. S. Feld, *Phys. Rev. Lett.*, 1997, **78**, 1667–1670.
- J. P. Camden, J. A. Dieringer, Y. M. Wang, D. J. Masiello, L. D. Marks, G. C. Schatz and R. P. Van Duyne, *J. Am. Chem. Soc.*, 2008, **130**, 12616–12617.
- K. Kneipp, H. Kneipp, G. Deinum, I. Itzkan, R. R. Dasari and M. S. Feld, *Appl. Spectrosc.*, 1998, **52**, 175–178.
- S. L. Kleinman, E. Ringe, N. Valley, K. L. Wustholz, E. Phillips, K. A. Scheidt, G. C. Schatz and R. P. Van Duyne, *J. Am. Chem. Soc.*, 2011, **133**, 4115–4122.
- C. S. Thaxton, R. Elghanian, A. D. Thomas, S. I. Stoeva, J.-S. Lee, N. D. Smith, A. J. H. Schaeffer, W. Horninger, G. Bartsch and C. A. Mirkin, *Proc. Natl. Acad. Sci. U. S. A.*, 2009, **106**(44), 18437–18442.
- J. A. Dieringer, R. B. Lettan II, K. A. Scheidt and R. P. Van Duyne, *J. Am. Chem. Soc.*, 2007, **129**, 16249.
- L. Gunnarsson, E. J. Bjerneld, H. Xu, S. Petronis, B. Kasemo and M. Kall, *Appl. Phys. Lett.*, 2001, **78**, 802–804.
- M. Mulvihill, A. Tao, K. Benjauthrit, J. Arnold and P. Yang, *Angew. Chem., Int. Ed.*, 2008, **47**, 6456–6460.
- W. Li, P. H. C. Camargo, L. Au, Q. Zhang, M. Rycenga and Y. Xia, *Angew. Chem., Int. Ed.*, 2010, **49**, 164–168.
- C. E. Talley, J. B. Jackson, C. Oubre, N. K. Grady, C. W. Hollars, S. M. Lane, T. R. Huser, P. Nordlander and N. J. Halas, *Nano Lett.*, 2005, **5**, 1569–1574.
- P. H. C. Camargo, M. Rycenga, L. Au and Y. Xia, *Angew. Chem., Int. Ed.*, 2009, **48**, 2180–2184.
- S.-C. Yang, H. Kobori, C.-L. He, M.-H. Lin, H.-Y. Chen, C. C. Li, M. Kanehara, T. Teranishi and S. Gwo, *Nano Lett.*, 2010, **10**, 632–637.
- J. M. McLellan, A. Seikkinen, J. Chen and Y. Xia, *Chem. Phys. Lett.*, 2006, **427**, 122–126.
- Y. Yang, S. Matsubara, L. Xiong, T. Hayakawa and M. Nogami, *J. Phys. Chem. C*, 2007, **111**, 9095–9104.
- M. Rycenga, M. H. Kim, P. H. C. Camargo, C. Cobley, Z.-Y. Li and Y. Xia, *J. Phys. Chem. A*, 2009, **113**, 3932–3939.
- Y. Lu, G. L. Liu and L. P. Lee, *Nano Lett.*, 2005, **5**, 5–9.
- J. M. McLellan, Z.-Y. Li, A. R. Siekkinen and Y. Xia, *Nano Lett.*, 2007, **7**, 1013–1017.
- M. A. Mahmoud, C. E. Tabor and M. A. El-Sayed, *J. Phys. Chem. C*, 2009, **113**, 5493–5501.
- S. Y. Lee, L. Hung, G. S. Lang, J. E. Cornett, I. D. Mayergoyz and O. Rabin, *ACS Nano*, 2010, **4**, 5763–5772.
- M. Rycenga, X. Xia, C. Moran, F. Zhou, D. Qin, Z.-Y. Li and Y. Xia, *Angew. Chem., Int. Ed.*, 2011, **50**, 5473–5477.
- H. L. Wu, H. R. Tsai, Y. T. Hung, K. U. Lao, C. W. Liao, P. J. Chung, J. S. Huang, I. C. Chen and M. H. Huang, *Inorg. Chem.*, 2011, **50**, 8106–8111.
- O. Rabin and S. Y. Lee, *J. Nanotechnol.*, 2012, **2012**.
- J. C. S. Costa, R. A. Ando, A. C. Sant'Ana, L. M. Rossi, P. S. Santos, M. L. A. Temperini and P. Corio, *Phys. Chem. Chem. Phys.*, 2009, **11**, 7491–7498.
- M. Saito, M. Shibasaki, S. Nakamura and M. Miyagi, *Opt. Lett.*, 1994, **19**, 710–712.
- K. H. A. Lau, L.-S. Tan, K. Tamada, M. S. Sander and W. Knoll, *J. Phys. Chem. B*, 2004, **108**, 10812–10818.
- S. Chang, H. Ko, S. Singamaneni, R. Gunawidjaja and V. V. Tsukruk, *Anal. Chem.*, 2009, **81**, 5740–5748.
- R. Kodiyath, J. Wang, Z. A. Combs, S. Chang, M. K. Gupta, K. D. Anderson, R. J. C. Brown and V. V. Tsukruk, *Small*, 2011, **7**, 3452–3457.
- R. Kodiyath, T. A. Papadopoulos, J. Wang, Z. A. Combs, H. Li, R. J. C. Brown, J.-L. Bredas and V. V. Tsukruk, *J. Phys. Chem. C*, 2012, **116**, 13917–13927.
- V. Dobrokhotov, L. Oakes, D. Sowell, A. Larin, J. Hall, A. Kengne, P. Bakharev, G. Corti, T. Cantrell, T. Prakash, J. Williams and D. N. McIlroy, *Sens. Actuators, B*, 2012, **168**, 138–148.
- W. Zhang, L.-G. Qiu, Y.-P. Yuan, A.-J. Xie, Y.-H. Shen and J.-F. Zhu, *J. Hazard. Mater.*, 2012, **221**, 147–154.
- L. Yang, L. Ma, G. Chen, J. Liu and Z. Q. Tian, *Chem.–Eur. J.*, 2010, **16**, 12683–12693.
- H. Ko and V. V. Tsukruk, *Small*, 2008, **4**, 1980–1984.
- H. Ko, S. Chang and V. V. Tsukruk, *ACS Nano*, 2009, **3**, 181–188.
- S. S. R. Dasary, A. K. Singh, D. Senapati, H. Yu and P. C. Ray, *J. Am. Chem. Soc.*, 2009, **131**, 13806–13812.
- Y. Li, N. Koshizaki, H. Q. Wang and Y. Shimizu, *ACS Nano*, 2011, **5**, 9403–9412.
- M. S. Schmidt and A. Boisen, *Advanced Environmental, Chemical, and Biological Sensing Technologies VII*, Orlando, Florida, USA, 2010.
- J. M. Sylvia, J. A. Janni, J. D. Klein and K. M. Spencer, *Anal. Chem.*, 2000, **72**, 5834–5840.
- Y. S. Li, T. Vodinh, D. L. Stokes and W. Yu, *Appl. Spectrosc.*, 1992, **46**, 1354–1357.
- R. Holze, *Electrochim. Acta*, 1990, **35**, 1037–1044.
- W. Ma and Y. Fang, *J. Colloid Interface Sci.*, 2006, **303**, 1–8.
- G. A. Bakken, G. W. Kauffman, P. C. Jurs, K. J. Albert and S. S. Stitzel, *Sens. Actuators, B*, 2001, **79**, 1–10.
- M. Snels, T. Venezia and L. Belfiore, *Chem. Phys. Lett.*, 2010, **489**, 134–140.
- A. D. Aguilar, E. S. Forzani, M. Leright, F. Tsow, A. Cagan, R. A. Iglesias, L. A. Nagahara, I. Amlani, R. Tsui and N. J. Tao, *Nano Lett.*, 2009, **10**, 380–384.
- Office of Naval Research. Combat Safe Insensitive Munitions Program, <http://www.onr.navy.mil/Science-Technology/Departments/Code-35/All-Programs/aerospace-research-351/Combat-Safe-Insensitive-Munitions.aspx> (accessed July 23, 2012).
- U.S. Army. Modernizing and Equipping the Force (Part 1), <http://www.army.mil/article/49954/> (accessed July 23, 2012), December 30, 2010.
- Global. Security. Insensitive Munitions, <http://www.globalsecurity.org/military/systems/munitions/im.htm> (accessed July 23, 2012).

- 49 Joint Requirements Oversight Council. Insensitive Munitions Certification Policy, <http://www.insensitivemunitions.org/wp-content/uploads/2011/06/annex3.jpg> (accessed July 23, 2012), The Joint Staff, Washington, DC, July 2, 2004.
- 50 D. W. Doll and N. Rasmussen, Impact resistant explosive compositions. *US Pat.*, 7,744,710, June 29, 2010.
- 51 J. A. Viccelli, L. L. Wood, M. Y. Ishikawa, J. H. Nuckolls and P. F. Pagoria, Explosively driven low-density foams and powders. *US Pat.*, 7,707,819, May 4, 2010.
- 52 W. C. Fleming, H. J. McSpadden and D. E. Olander, Ammonium nitrate propellants and methods for preparing the same. *US Pat.*, 6, 913,66, July 5, 2005.
- 53 P. W. Benard, F. C. Fouche and H. C. Bezuidenhout, *Australian Explosive Ordnance Symposium (Parari' 1997)*, 1997, p. 12.
- 54 J. P. Agrawal and R. D. Hodgson, *Organic Chemistry of Explosives*, John Wiley & Sons, Chichester, 2007.
- 55 S. Nicolish, J. Niles, P. Ferlazzo, D. Doll, P. Braithwaite, N. Rasmussen, M. Ray, M. Gunger and A. Spencer, *Recent developments in reduced sensitivity melt pour explosives, 34th Int. Ann. Conf. of ICT*, Karlsruhe, Germany, 24–27th June 2003, pp. 135(1)–135(21).
- 56 R. K. Toghiani, H. Toghiani, S. W. Maloney and V. M. Boddu, in *Energetic Materials: Thermophysical Properties, Predictions, and Experimental Measurements*, ed. V. Boddy and P. Redner, Taylor and Francis Group, LLC, 2011, pp. 171–195.
- 57 S. Chang, Z. A. Combs, M. K. Gupta, R. Davis and V. V. Tsukruk, *ACS Appl. Mater. Interfaces*, 2010, 2, 3333–3339.
- 58 M. A. Mahmoud and M. A. El-Sayed, *J. Phys. Chem. C*, 2008, 112, 14618–14625.
- 59 M. Lahav, T. Schayek, A. Vaskevich and I. Rubinstein, *Angew. Chem., Int. Ed.*, 2003, 42, 5575–5579.
- 60 M. L. Bruening, D. M. Dotzauer, P. Jain and G. L. Baker, *Langmuir*, 2008, 24, 7663–7673.
- 61 C. Jiang and V. V. Tsukruk, *Adv. Mater.*, 2006, 18, 829–840.
- 62 V. V. Tsukruk, *Prog. Polym. Sci.*, 1997, 22, 247–311.
- 63 W. Lee, R. Scholz, K. Nielsch and U. Gosele, *Angew. Chem., Int. Ed.*, 2005, 44, 6050–6054.
- 64 X. Fang and S. R. Ahmad, *Appl. Phys. B: Lasers Opt.*, 2009, 97, 723–726.
- 65 M. K. K. Oo, Y. Guo, K. Reddy, J. Liu and X. Fan, *Anal. Chem.*, 2012, 84, 3376–3381.
- 66 S. Singamaneni, M. Gupta, R. Yang, M. M. Tomczak, R. R. Naik, Z. L. Wang and V. V. Tsukruk, *ACS Nano*, 2009, 3, 2593–2600.
- 67 M. J. Frisch, G. W. Trucks, H. B. Schlegel, G. E. Scuseria, M. A. Robb, J. R. Cheeseman, J. A. Montgomery Jr, T. Vreven, K. N. Kudin and J. C. Burant, *et al.*, *Gaussian 03, Revision. C.06*, Gaussian, Inc., Wallingford CT, 2004.
- 68 A. Taflove, *Computational Electrodynamics - The Finite Difference Time-domain Method*, Artech House, 1995.
- 69 K. S. Yee, *IEEE trans. on Antennas and Propagation ap-14*, 1966, 302.
- 70 M. A. Mahmoud, M. Chamanza, A. Adibi and M. A. El-Sayed, *J. Am. Chem. Soc.*, 2012, 134, 6434–6442.
- 71 N. Grillet, D. Manchon, F. Bertorelle, C. Bonnet, M. Broyer, E. Cottancin, J. Lermé, M. Hillenkamp and M. Pellarin, *ACS Nano*, 2011, 12, 9450–9462.
- 72 W. M. Haynes, *CRC Handbook of Chemistry and Physics*, CRC PRESS, 81st edn, 2000.
- 73 E. D. Palik, *Handbook of Optical Constants of Solids*, Academic Press, New York, 1985.
- 74 J. Aizenberg, P. V. Braun and P. Wiltzius, *Phys. Rev. Lett.*, 2000, 84, 2997–3000.
- 75 G. M. Bell, S. Levine and L. N. McCartney, *J. Colloid Interface Sci.*, 1970, 33, 335–359.
- 76 B. Gao, G. Arya and A. R. Tao, *Nat. Nanotechnol.*, 2012, 7, 433–437.
- 77 C. M. Cobley, M. Rycenga, F. Zhou, Z. Y. Li and Y. Xia, *J. Phys. Chem. C*, 2009, 113, 16975–16982.
- 78 J. Hohlbein, U. Rehn and R. B. Wehrspohn, *Phys. Status Solidi A*, 2004, 201, 806–810.
- 79 J. J. Mock, D. R. Smith and S. Schultz, *Nano Lett.*, 2003, 3, 485–491.
- 80 C. L. Haynes and R. P. Van Duyne, *J. Phys. Chem. B*, 2003, 107, 7426–7433.
- 81 R. A. Alvarez-Puebla, D. S. Santos Jr and R. F. Aroca, *Analyst*, 2007, 132, 1210–1214.
- 82 K. B. Biggs, J. P. Camden, J. N. Anker and R. P. Van Duyne, *J. Phys. Chem. A*, 2009, 113, 4581–4586.
- 83 W. Ma and Y. Fang, *J. Colloid Interface Sci.*, 2006, 303, 1–8.
- 84 D. D. Kulkarni, S. Kim, A. G. Fedorov and V. V. Tsukruk, *Adv. Funct. Mater.*, 2012, 22, 2129–2139.
- 85 M. A. Mahmoud, F. Saira and M. A. El-Sayed, *Nano Lett.*, 2010, 10, 3764–3769.
- 86 Yi. Lin, C. E. Bunker, K. A. Fernando and J. W. Connel, *ACS Appl. Mater. Interfaces*, 2012, 4, 1110–1117.
- 87 P. Aldeanueva-Potel, E. Faoucher, R. A. Alvarez-Puebla, L. M. Liz-Marzan and M. Brust, *Anal. Chem.*, 2009, 81, 9233–9238.
- 88 Y. Han, R. Lupitskyy, T. M. Chou, C. M. Stafford, H. Du and S. Sukhishvili, *Anal. Chem.*, 2011, 83(15), 5873–5880.